Journal of Computational and Applied Mathematics 428 (2023) 115209

Contents lists available at ScienceDirect

Journal of Computational and Applied Mathematics

journal homepage: www.elsevier.com/locate/cam

Momentum Weighted Interpolation for unsteady weakly compressible two-phase flows on unstructured meshes

Giuseppe Sirianni [a,*], Barbara Re [a], Remi Abgrall [b], Alberto Guardone [a]

[a] Department of Aerospace Science and Technology, Politecnico di Milano, Via La Masa 34, 20156, Milan, Italy
[b] Institute of Mathematics, University of Zurich, Winterthurerstrasse 190, CH-8057, Zurich, Switzerland

ARTICLE INFO

Article history:
Received 31 October 2022
Received in revised form 16 February 2023

Keywords:
Baer–Nunziato
Weakly compressible
Multiphase
Unstructured
Rhie-Chow
Momentum Weighted Interpolation

ABSTRACT

A set of strategies and numerical techniques for simulating weakly compressible two-phase flows is presented. A pressure formulation of the full Baer–Nunziato equations with arbitrary equation of state is presented. Node centered finite volumes are used on unstructured meshes in a fully implicit solver. To mitigate the pressure checkerboarding that arises from the collocated variable arrangement, a Momentum Weighted Interpolation formulation is derived specifically for the Baer–Nunziato equations. The proposed approach is thoroughly tested against analytic and experimental data.

1. Introduction

This paper is a first step towards extending the work done by Re and Abgrall [1] on the development of a new pressure-based formulation of the Baer–Nunziato model [2] for weakly compressible applications, such as the transport of CO_2 for the carbon capture and storage (CCS) process [3,4]. Various pressure-based models exist for the volume of fluid approach [5,6] and for a simplified Kapila model [7]. We chose the model by Re and Abgrall [1] as it allows for arbitrary equations of state (EoSs) and is, to our knowledge, the only pressure-based approach for a full disequilibrium Baer–Nunziato type model. The aim of the present paper is to extend their 1D work to multidimensional unstructured grids, within the simulation framework provided by the open-source software suite SU2 [8]. In this paper, we will only consider the hyperbolic part of the model and neglect the relaxation terms.

One of the main problems that arise when moving from a 1D staggered approach to a multidimensional unstructured collocated variable arrangement in the weakly compressible regime is pressure checkerboarding [9]. This phenomenon can be circumvented by using a staggered variable arrangement [10,11] which can be fairly straightforward for structured meshes, but is more difficult to implement over unstructured meshes [12,13] and which also adds to the computational cost. Another popular approach used to mitigate pressure checkerboarding is the Rhie & Chow interpolation [14,15], also known as the Momentum Weighted Interpolation (MWI). This approach has found great success, particularly in many unstructured codes such as OpenFOAM [16]. MWI has been studied for both single [17–19] and multiphase [20–23] flows, but there is no formulation in the literature for the Baer–Nunziato model. For this paper, we, therefore, derive a new formulation of the Rhie & Chow correction [14] specific for the Baer–Nunziato equations, following a procedure inspired by the one in Bartholomew et al. [24]. Due to its importance in avoiding spurious oscillations across multi-material interfaces, the pressure and velocity non-disturbance condition [25] is preserved by the proposed Rhie & Chow correction.

* Corresponding author.
E-mail address: giuseppe.sirianni@polimi.it (G. Sirianni).

https://doi.org/10.1016/j.cam.2023.115209
0377-0427/

The governing equations are discretized following the finite-volume approach by Re and Abgrall [1] wherever possible, but some adaptation is required since we are using a collocated variable arrangement on a multidimensional unstructured mesh instead of a 1D staggered approach. We integrate in time implicitly to overcome the acoustic limitation posed on the timestep that in the weakly compressible regime may become very stringent.

This work's main aim is to present the most straightforward extension of the 1D model by Re & Abgrall [1] to a collocated unstructured solver making use of the framework of tools provided by the open-source software suite SU2 [8]. Since we decided to move from a staggered variable arrangement, we need an alternative way of dealing with the pressure checkerboarding problem. For this reason we derive a Momentum Weighted Interpolation specifically for the Baer–Nunziato equations to dampen such oscillations. We also showcase the capabilities of said model to work outside the weakly compressible regime.

The paper starts with an outline on the conservation laws in Section 2, followed by the numerical discretization in Section 3, with the Momentum Weighted Interpolation derived in Section 3.1.1. Numerical results obtained using the developed solver are then presented. Since the solver has been built from the ground up for this work, we first show its validity by performing a pure advection test to check that the non-disturbance condition is fulfilled in Section 4.1, and a no-mixing shock tube test to check time and space convergence to the entropic solution in Section 4.2. Then, the effectiveness of the MWI formulation is assessed in a custom-built multiphase test involving a helium slip bubble in Section 4.3, and in the Helium shock interaction test in the compressible regime, for which experimental results are available, in Section 4.4. Finally, conclusions are drawn in Section 5.

2. Model

In this section, we recall the model by Re & Abgrall [1] which is used in this paper to model full disequilibrium two-phase flows in the weakly compressible regime. In this regime, the reference Mach number M_r tends to zero, so the classical adimensional momentum equation presents a singularity ($1/M_r^2$) in front of the pressure gradient. This can be avoided using a particular pressure scaling as done by Wenneker et al. [26]. This scaling was originally applied to the 1D Baer–Nunziato equations by Re and Abgrall [1]. First, we define the reference dimensional variables $(\cdot)_r$, as in Eq. (1), where ρ is the density, U is the speed, P is the pressure, t is the time, and L is the length.

$$\rho_r \qquad U_r \qquad P_r \qquad M_r^2 = \frac{\rho_r U_r^2}{P_r} \qquad t_r = \frac{L_r}{U_r} \tag{1}$$

We denote with the subscript $(\cdot)_k$ the kth phase quantity, α the volume fraction, $\alpha\rho$ the density, $\alpha\rho\underline{\boldsymbol{u}}$ the momentum, and P the pressure. Also, $\tilde{(\cdot)}$ denotes dimensional quantities and $(\cdot)$ adimensional ones. We define the interfacial velocity $\underline{\tilde{\boldsymbol{u}}}_I$ and interfacial pressure $\tilde{P}_I$ as

$$\underline{\tilde{\boldsymbol{u}}}_I = \frac{\sum_k \alpha_k \tilde{\rho}_k \underline{\tilde{\boldsymbol{u}}}_k}{\sum_k \alpha_k \tilde{\rho}_k} \qquad \tilde{P}_I = \sum_k \alpha_k \tilde{P}_k. \tag{2}$$

Let us now define for an arbitrary EoS the following dimensional thermodynamic quantities ($\tilde{c}_k$ is the speed of sound and $\tilde{e}_k$ is the internal energy per unit of volume) and derivatives ($\tilde{\chi}_k$ and $\tilde{\kappa}_k$), as they will be later needed to define an equation for the evolution of the phasic pressure.

$$\tilde{c}_k^2 = \tilde{\chi}_k + \tilde{\kappa}_k \frac{\tilde{P}_k + \tilde{e}_k}{\tilde{\rho}_k} \qquad \tilde{\kappa}_k = \left(\frac{\partial \tilde{P}_k}{\partial \tilde{e}_k}\right)_{\tilde{\rho}_k} \qquad \tilde{\chi}_k = \left(\frac{\partial \tilde{P}_k}{\partial \tilde{\rho}_k}\right)_{\tilde{e}_k}. \tag{3}$$

By analogy with the form of the speed of sound, a dimensional interfacial speed of sound $\tilde{c}_{I,k}$ is defined as $\tilde{c}_{I,k}^2 = \tilde{\chi}_k + \tilde{\kappa}_k \frac{\tilde{P}_I + \tilde{e}_k}{\tilde{\rho}_k}$. This is not a thermodynamic quantity but it is useful to write the phasic pressure evolution equation. Now, all dimensionless quantities $(\cdot)$ can be computed from their dimensional counterpart $\tilde{(\cdot)}$ as in Eq. (4). More details on the derivation can be found in the original paper by Re & Abgrall [1].

$$\begin{aligned} P_k &= \frac{\tilde{P}_k - P_r}{\rho_r U_r^2} & \underline{\boldsymbol{u}}_k &= \frac{\underline{\tilde{\boldsymbol{u}}}_k}{U_r} & \rho_k &= \frac{\tilde{\rho}_k}{\rho_r} & e_k &= \frac{\tilde{e}_k}{\rho_r U_r^2} & t &= \frac{\tilde{t}}{t_r} \\ \chi_k &= \frac{\tilde{\chi}_k}{U_r^2} & \kappa_k &= \tilde{\kappa}_k & c_{I,k}^2 &= \frac{\tilde{c}_{I,k}^2}{U_r^2} - \frac{1}{M_r^2}\frac{\kappa_k}{\rho_k} & c_k^2 &= \frac{\tilde{c}_k^2}{U_r^2} - \frac{1}{M_r^2}\frac{\kappa_k}{\rho_k} & x &= \frac{\tilde{x}}{L_r} \end{aligned} \tag{4}$$

Finally, the dimensionless Re & Abgrall [1] pressure formulation of the Baer–Nunziato equations [2] is defined as in Eq. (5). We maintain the definition of the interface quantities identical to Eq. (2) but we compute them with the dimensionless counterparts of all the variables (e.g. $P_I = \sum_k \alpha_k P_k$). Note that there is one of each of these equations for each phase, except for the volume fraction equation where the last phase's volume fraction can be simply computed

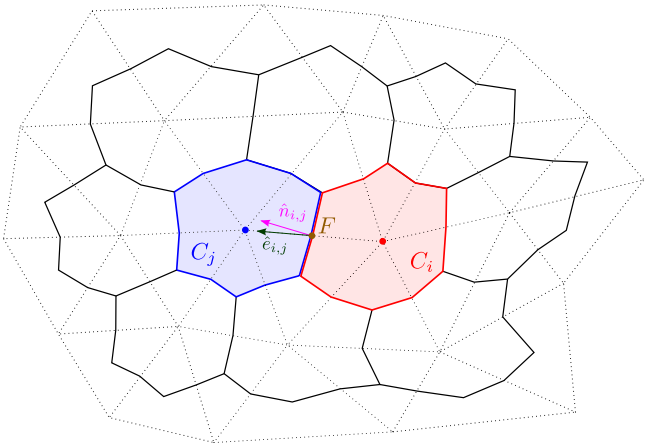

Fig. 1. Node centered finite volume control volume sketch.

as $\alpha_{N_{phases}} = 1 - \sum_{k=1}^{N_{phases}-1} \alpha_k$.

$$\begin{cases} \dfrac{\partial \alpha_k}{\partial t} & + \underline{\boldsymbol{u}}_I \cdot \overline{\nabla} \alpha_k = 0 \\ \dfrac{\partial \alpha_k \rho_k}{\partial t} & + \overline{\nabla} \cdot \left(\alpha_k \rho_k \underline{\boldsymbol{u}}_k \right) = 0 \\ \dfrac{\partial \alpha_k \rho_k \underline{\boldsymbol{u}}_k}{\partial t} & + \overline{\nabla} \cdot \left(\alpha_k \rho_k \underline{\boldsymbol{u}}_k \otimes \underline{\boldsymbol{u}}_k + \alpha_k P_k \underline{\underline{\boldsymbol{I}}} \right) - P_I \overline{\nabla} \alpha_k = \underline{\boldsymbol{0}} \\ M_r^2 \alpha_k \left(\dfrac{\partial P_k}{\partial t} \right. & \left. + \underline{\boldsymbol{u}}_k \cdot \overline{\nabla} P_k \right) + \left(M_r^2 \alpha_k \rho_k c_k^2 + \kappa_k \alpha_k \right) \overline{\nabla} \cdot \underline{\boldsymbol{u}}_k - \left(M_r^2 \rho_k c_{I,k}^2 + \kappa_k \right) \left(\underline{\boldsymbol{u}}_I - \underline{\boldsymbol{u}}_k \right) \cdot \overline{\nabla} \alpha_k = 0 \end{cases} \tag{5}$$

As in the original work [1], the model is written in primitive variables and therefore conservation or convergence to the weak solution are not guaranteed. These equations are agnostic to the choice of the equation of state, as long as it can be expressed in the form $\tilde{e}_k = \tilde{e}_k(\tilde{\rho}_k, \tilde{P}_k)$. For this particular work, we used the stiffened gas EoS [27], which is the simplest model able to describe attractive and repulsive molecular effects, suitable for both liquids and gases. Its pressure EoS reads

$$\tilde{P}_k(\tilde{e}_k, \tilde{\rho}_k) = (\tilde{\gamma}_k - 1) \left[\tilde{e}_k - \tilde{\rho}_k \tilde{q}_{0,k} \right] - \tilde{\gamma}_k \tilde{P}_{\infty,k}, \tag{6}$$

where $\tilde{P}_{\infty,k}$ and $\tilde{q}_{0,k}$ are gas-specific constants, which can be determined by fitting experimental data [28]. Note that if $\tilde{P}_{\infty,k} = 0$ and $\tilde{q}_{0,k} = 0$, the stiffened gas EoS devolves into the ideal gas EoS. The thermodynamic quantities and derivatives for the stiffened gas EoS in the dimensional form are computed from Eq. (6) in Eq. (7), and the adimensional scaling is done by following Eq. (4). Here $c_{v,k}$ is the specific heat capacity at constant volume, T_k is the temperature and γ_k is the specific heat ratio.

$$\tilde{e}_k = \frac{\tilde{P}_k + \tilde{\gamma}_k \tilde{P}_{\infty,k}}{(\tilde{\gamma}_k - 1)} + \tilde{\rho}_k \tilde{q}_{0,k} \qquad \tilde{\chi}_k = -(\tilde{\gamma}_k - 1)\, \tilde{q}_{0,k} \qquad \tilde{\kappa}_k = (\tilde{\gamma}_k - 1) \qquad \tilde{T}_k = \frac{\tilde{P}_k + \tilde{P}_{\infty,k}}{\tilde{\rho}_k \tilde{c}_{v,k} (\tilde{\gamma}_k - 1)} \tag{7}$$

3. Numerical discretization

In this section we describe the time implicit, finite volume, node-centered, dual-mesh, edge-based approach we use to numerically discretize and solve Eq. (5) within the open source software SU2 [8]. Conservative terms are discretized using pseudo-Rusanov fluxes and non-conservative terms are discretized using central difference schemes unless otherwise specified (Section 3.1). To mitigate pressure checkerboarding, the divergence of the velocity is discretized by not using a central difference scheme but using a Momentum Weighted Interpolated (MWI) velocity derived specifically in this work for the Baer–Nunziato pressure formulation [1] (Section 3.1.1). To advance the unsteady simulation in time, a pseudo-Newton–Raphson strategy is applied following the standard tools and procedures found in SU2 [8] (see Section 3.2). Control volumes (CVs) are constructed around the primary mesh' nodes as depicted in Fig. 1. We also depict the unit normal $\hat{\boldsymbol{n}}_{i,j}$ and the unit vector $\hat{\boldsymbol{e}}_{i,j}$ along the edge between the control volumes C_i and C_j, which will be useful later.

We report the space–time discrete form of the integral form of a general system of conservation equations over the ith CV (C_i) in Eq. (8) before defining the residuals. Quantities related to the ith CV are denoted $(\cdot)_i$, quantities related to its jth CV are denoted $(\cdot)_j$ and quantities related to the current t^n and the next t^{n+1} time step are denoted $(\cdot)^n$ and $(\cdot)^{n+1}$

respectively. Note that $\underline{\boldsymbol{q}}_i^n$ is the vector of variables we are solving for at time t^n in C_i, $|C_i|$ is the CV's volume, $A_{i,j}$ is the area shared between C_i and C_j, $\underline{\boldsymbol{S}}(\underline{\boldsymbol{q}}_i^{n+1})$ is the vector of non-conservative terms computed in C_i, $\underline{\boldsymbol{F}}_{i,j}^{cons}$ is the conservative numerical flux computed between C_i and C_j, $\underline{\boldsymbol{R}}_i$ is the residual at node i. The definition of $\underline{\boldsymbol{R}}_i$ is important for the implicit time discretization that will be briefly described in Section 3.2.

$$\underline{\boldsymbol{R}}_i^{n+1} = |C_i| \frac{\underline{\boldsymbol{q}}_i^{n+1} - \underline{\boldsymbol{q}}_i^n}{\Delta t} + \sum_{C_j \in \partial C_i} A_{i,j} \underline{\boldsymbol{F}}_{i,j}^{cons} - |C_i| \underline{\boldsymbol{S}}(\underline{\boldsymbol{q}}_i^{n+1}) = \underline{\boldsymbol{0}} \tag{8}$$

Since non-conservative terms of Eq. (5) are all gradient terms, and we will be using the Green–Gauss theorem to discretize them, it is useful to rewrite the non-conservative contribution $|C_i|\underline{\boldsymbol{S}}(\underline{\boldsymbol{q}}_i^{n+1})$ of Eq. (8) as a boundary integral. To do so we recall the Green–Gauss theorem for a generic quantity f.

$$\overline{\nabla} f \Big|_{C_i} = \frac{1}{|C_i|} \oint_{\partial C_i} f \hat{\boldsymbol{n}} ds \simeq \frac{1}{|C_i|} \sum_{C_j \in \partial C_i} A_{i,j} \left(f_i + f_j\right) \hat{\boldsymbol{n}}_{i,j} \tag{9}$$

If we assume that all terms multiplying the gradients in the non-conservative term are constant within a CV, we can take them out of the integral and therefore rewrite the residual from Eq. (8) as.

$$\underline{\boldsymbol{R}}_i^{n+1} = |C_i| \frac{\underline{\boldsymbol{q}}_i^{n+1} - \underline{\boldsymbol{q}}_i^n}{\Delta t} + \sum_{C_j \in \partial C_i} A_{i,j} \left(\underline{\boldsymbol{F}}_{i,j}^{cons} + \underline{\boldsymbol{F}}_{i,j}^{non-cons}\right) = \underline{\boldsymbol{0}} \tag{10}$$

3.1. Space discretization

In this section, we define the spatial residuals used in this work, for both conservative and non-conservative terms. The discretization of the boundary integral $(\sum A_{i,j} \left(\underline{\boldsymbol{F}}_{i,j}^{cons} + \underline{\boldsymbol{F}}_{i,j}^{non-cons}\right))$ outlined previously in Eq. (10) is specified in Eq. (13) for each equation using the naming scheme defined in Eq. (11). To ease the notation the subscript $(\cdot)_k$ denoting the phase as been dropped from here on. All subscripts now denote to which CV the quantities are referred to.

$$\begin{aligned}
&\textit{Volume Fraction} && \int_{C_i} \underline{\boldsymbol{u}}_I \cdot \overline{\nabla} \alpha dV && \simeq \sum_{C_j \in \partial C_i} A_{i,j} F_{i,j}^{non-cons\ [\alpha]} \\
&\textit{Mass} && \int_{\partial C_i} \alpha \rho \underline{\boldsymbol{u}} \cdot \hat{\boldsymbol{n}} ds && \simeq \sum_{C_j \in \partial C_i} A_{i,j} F_{i,j}^{cons\ [\alpha\rho]} \\
&\textit{Momentum} && \int_{\partial C_i} \left(\alpha \rho \underline{\boldsymbol{u}} \otimes \underline{\boldsymbol{u}} + \alpha P \underline{\underline{\boldsymbol{I}}}\right) \cdot \hat{\boldsymbol{n}} ds - \int_{C_i} P_I \overline{\nabla} \alpha dV && \simeq \sum_{C_j \in \partial C_i} A_{i,j} \left(\underline{\boldsymbol{F}}_{i,j}^{cons\ [\alpha\rho\underline{\boldsymbol{u}}]} + \underline{\boldsymbol{F}}_{i,j}^{non-cons\ [\alpha\rho\underline{\boldsymbol{u}}]}\right) \\
&\textit{Pressure} && \int_{C_i} M_r^2 \alpha \underline{\boldsymbol{u}} \cdot \overline{\nabla} P dV + \int_{C_i} \left(M_r^2 \alpha c^2 + \kappa \alpha\right) \overline{\nabla} \cdot \underline{\boldsymbol{u}} dV && \\
& && - \int_{C_i} \left(M_r^2 c_I^2 + \kappa\right) \left(\underline{\boldsymbol{u}}_I - \underline{\boldsymbol{u}}\right) \cdot \overline{\nabla} \alpha dV && \simeq \sum_{C_j \in \partial C_i} A_{i,j} F_{i,j}^{non-cons\ [P]}
\end{aligned} \tag{11}$$

The conservative fluxes for mass and momentum are discretized using pseudo Rusanov [29] fluxes, using the local velocity $\lambda = |\underline{\boldsymbol{u}} \cdot \hat{\boldsymbol{n}}|$ instead of the eigenvalue $\lambda = |\underline{\boldsymbol{u}} \cdot \hat{\boldsymbol{n}}| + c$ as it was the most natural path to extend the work from Re & Abgrall [1]:

$$\underline{\boldsymbol{F}}_{i,j}^{cons} = \frac{1}{2} \left(\underline{\boldsymbol{F}}(\underline{\boldsymbol{q}}_i) + \underline{\boldsymbol{F}}(\underline{\boldsymbol{q}}_i)\right) - \frac{1}{2} \max_{i,j} (\lambda) \left(\underline{\boldsymbol{q}}_j - \underline{\boldsymbol{q}}_i\right) \tag{12}$$

The discretization of the non-conservative terms involving the gradient of the volume fraction is a critical point in any numerical scheme for compressible multi-phase flows. Indeed, oscillations and other computational inaccuracies may originate across multi-material interfaces if the pressure equilibrium among the different components is not properly addressed [30]. To reach this, we will follow the so-called non-disturbance condition by Abgrall [25], which states that, to avoid spurious oscillations across multi-material interfaces, a flow field uniform in pressure and velocity should be preserved exactly by the numerical discretization as time evolves. The fulfillment of this condition is guaranteed by constructing accurately the discretization of the non-conservative terms [31]. As a result, the discretizations of the phase coupling terms in the volume fraction and pressure equations resemble the pseudo-Rusanov fluxes used for the convective terms, with a central and an upwind term, but with a slightly different choice for the velocities, as shown in (13). The pressure gradient term in the pressure equation has a similar expression, reported in (13), but the reason is different: while integrating this term over the cell C_i, the velocity that pre-multiplies the pressure gradient can be approximated as constant and equal to the velocity in that cell, i.e., $\underline{\boldsymbol{u}}_i$. All other gradient terms are computed using central differences

(also the non conservative momentum term, see Appendix A) except the velocity divergence in the pressure equation which uses MWI as described in Section 3.1.1.

$$
\begin{aligned}
&\textit{Volume Fraction} && F_{i,j}^{non-cons\ [\alpha]} = \frac{1}{2}\left(\underline{\boldsymbol{u}}_{I,i}\cdot\hat{\boldsymbol{n}}_{i,j}\right)\left[\alpha_i+\alpha_j\right] - \frac{1}{2}|\underline{\boldsymbol{u}}_{I,i}\cdot\hat{\boldsymbol{n}}_{i,j}|\left[\alpha_j-\alpha_i\right]\\
&\textit{Mass} && F_{i,j}^{cons\ [\alpha\rho]} = \frac{1}{2}\left[\alpha\rho\underline{\boldsymbol{u}}_i\cdot\hat{\boldsymbol{n}}_{i,j}+\alpha\rho\underline{\boldsymbol{u}}_j\cdot\hat{\boldsymbol{n}}_{i,j}\right]\\
&&& \quad -\frac{1}{2}\max_{i,j}\left(|\underline{\boldsymbol{u}}_i\cdot\hat{\boldsymbol{n}}_{i,j}|,|\underline{\boldsymbol{u}}_j\cdot\hat{\boldsymbol{n}}_{i,j}|\right)\left[\alpha\rho_j-\alpha\rho_i\right]\\
&\textit{Momentum} && \underline{\boldsymbol{F}}_{i,j}^{cons\ [\alpha\rho\underline{\boldsymbol{u}}]} = \frac{1}{2}\left[\alpha\rho\underline{\boldsymbol{u}}_i\left(\underline{\boldsymbol{u}}_i\cdot\hat{\boldsymbol{n}}_{i,j}\right)+\alpha_iP_i\hat{\boldsymbol{n}}_{i,j}+\alpha\rho\underline{\boldsymbol{u}}_j\left(\underline{\boldsymbol{u}}_j\cdot\hat{\boldsymbol{n}}_{i,j}\right)+\alpha_jP_j\hat{\boldsymbol{n}}_{i,j}\right]\\
&&& \quad -\frac{1}{2}\max_{i,j}\left(|\underline{\boldsymbol{u}}_i\cdot\hat{\boldsymbol{n}}_{i,j}|,|\underline{\boldsymbol{u}}_j\cdot\hat{\boldsymbol{n}}_{i,j}|\right)\left[\alpha\rho\underline{\boldsymbol{u}}_j-\alpha\rho\underline{\boldsymbol{u}}_i\right]\\
&&& \underline{\boldsymbol{F}}_{i,j}^{non-cons\ [\alpha\rho\underline{\boldsymbol{u}}]} = -\frac{1}{2}\left(\alpha_i+\alpha_j\right)P_{I,i}\hat{\boldsymbol{n}}_{i,j}\\
&\textit{Pressure} && F_{i,j}^{non-cons\ [P]} = M_r^2\alpha_i\left\{\frac{1}{2}\left[\left(\underline{\boldsymbol{u}}_i\cdot\hat{\boldsymbol{n}}_{i,j}\right)\left(P_i+P_j\right)\right]-\frac{1}{2}|\underline{\boldsymbol{u}}_i\cdot\hat{\boldsymbol{n}}_{i,j}|\left[P_j-P_i\right]\right\}\\
&&& \quad +\left(M_r^2\alpha_ic_i^2+\kappa_i\alpha_i\right)\left[\underline{\boldsymbol{u}}_F\cdot\hat{\boldsymbol{n}}_{i,j}\right]\\
&&& \quad +\left(M_r^2c_{I,i}^2+\kappa_i\right)\left\{\frac{1}{2}\left(\left(\underline{\boldsymbol{u}}_{I,i}-\underline{\boldsymbol{u}}_i\right)\cdot\hat{\boldsymbol{n}}_{i,j}\right)\left[\alpha_i+\alpha_j\right]\right.\\
&&& \quad \left.-\frac{1}{2}\left|\left(\underline{\boldsymbol{u}}_{I,i}-\underline{\boldsymbol{u}}_i\right)\cdot\hat{\boldsymbol{n}}_{i,j}\right|\left[\alpha_j-\alpha_i\right]\right\}
\end{aligned}
\tag{13}
$$

The face velocity $\underline{\boldsymbol{u}}_F$ used to compute the velocity divergence term in the pressure equation can be one of two reported in Eq. (14). The Momentum Weighted Interpolated (MWI) face velocity $\underline{\boldsymbol{u}}_F^{MWI}$ will be derived in Section 3.1.1 with the goal of suppressing pressure checkerboarding, and its final form can be found in Eq. (21).

$$
\begin{aligned}
&\underline{\boldsymbol{u}}_F = \frac{1}{2}\left(\underline{\boldsymbol{u}}_i+\underline{\boldsymbol{u}}_j\right) && \text{if using central differences}\\
&\underline{\boldsymbol{u}}_F = \underline{\boldsymbol{u}}_F^{MWI} && \text{if using Momentum Weighted Interpolation}
\end{aligned}
\tag{14}
$$

3.1.1. Momentum weighted interpolation

In this section, we derive the MWI face velocity $\underline{\boldsymbol{u}}_F^{MWI}$ for a pair of CVs C_i and C_j using a procedure similar to Bartholomew et al. [24]. This procedure, called Momentum Weighted Interpolation (also known as Rhie & Chow interpolation [14]), mimics a staggered variable arrangement by deriving a velocity from an imaginary momentum conservation equation written on an imaginary staggered control volume, centered on the face F between the CVs C_i and C_j (see Fig. 1). This should in principle mitigate the well-known pressure checkerboard problem that may arise in co-located schemes at low Mach numbers while removing the complexity of using a staggered variable arrangement on an unstructured mesh. The oscillations arise from the central differences in the pressure gradient (momentum equation) and velocity divergence (pressure equation).

The discrete equations for the momentum conservation over two neighboring control volumes C_i and C_j can be rewritten as Eq. (15), regardless of the discretization we are using. Note that $(\cdot)_i$ and $(\cdot)_j$ indicate what CV that term refers to. Also subscript $(\cdot)_{k(i)}$ refers to the CV C_k neighboring C_i. This is done by lumping in single coefficients (B_i^{n+1}, T_i^{n+1}, T_i^n) various terms according to what variable they multiply and from what term's discretization they arise from. In T_i^{n+1} and T_i^n we lump everything that comes from the time derivative discretization and that multiplies $\underline{\boldsymbol{u}}_i^{n+1}$ and $\underline{\boldsymbol{u}}_i^n$ respectively. In B_i^{n+1} we lump everything that comes from the conservative term discretization and that multiplies $\underline{\boldsymbol{u}}_i^{n+1}$.

$$
\begin{aligned}
&|C_i|T_i^{n+1}\underline{\boldsymbol{u}}_i^{n+1}+|C_i|T_i^n\underline{\boldsymbol{u}}_i^n+B_i^{n+1}\underline{\boldsymbol{u}}_i^{n+1}+\sum_{C_k\in\partial C_i}B_{k(i)}^{n+1}\underline{\boldsymbol{u}}_{k(i)}^{n+1}+|C_i|\overline{\nabla}\left(\alpha P\right)_i-|C_i|P_{I,i}\overline{\nabla}\left(\alpha\right)_i &&= \underline{\boldsymbol{0}}\\
&|C_j|T_j^{n+1}\underline{\boldsymbol{u}}_j^{n+1}+|C_j|T_j^n\underline{\boldsymbol{u}}_j^n+B_j^{n+1}\underline{\boldsymbol{u}}_j^{n+1}+\sum_{C_k\in\partial C_j}B_{k(j)}^{n+1}\underline{\boldsymbol{u}}_{k(j)}^{n+1}+|C_j|\overline{\nabla}\left(\alpha P\right)_j-|C_j|P_{I,j}\overline{\nabla}\left(\alpha\right)_j &&= \underline{\boldsymbol{0}}.
\end{aligned}
\tag{15}
$$

To ease the derivation, we define some auxiliary quantities in Eq. (16) by lumping various terms appearing in the discrete momentum Eqs. (15), as done by Bartholomew et al. [24]. Each of these auxiliary quantities is then referred to its control volume through the subscript $(\cdot)_i$ or $(\cdot)_j$.

$$
\begin{aligned}
&\tilde{\underline{\boldsymbol{u}}}_i = -\frac{1}{B_i^{n+1}}\textstyle\sum_{C_k\in\partial C_i}B_{k(i)}^{n+1}\underline{\boldsymbol{u}}_{k(i)}^{n+1}\\
&d_i = \frac{|C_i|}{B_i^{n+1}} \qquad \rightarrow \quad t_i = d_i\cdot T_i^n \qquad m_i = d_i\cdot T_i^{n+1}+1 \qquad g_i = d_i\cdot P_{I,i}
\end{aligned}
\tag{16}
$$

Then, after dividing them by B_i^{n+1} and B_j^{n+1} respectively, the momentum Eqs. (15) can be written as

$$\begin{aligned} m_i \underline{\boldsymbol{u}}_i^{n+1} &= \underline{\tilde{\boldsymbol{u}}}_i - d_i \overline{\nabla}(\alpha P)_i + g_i \overline{\nabla}(\alpha)_i - t_i \underline{\boldsymbol{u}}_i^n \\ m_j \underline{\boldsymbol{u}}_j^{n+1} &= \underline{\tilde{\boldsymbol{u}}}_j - d_j \overline{\nabla}(\alpha P)_j + g_j \overline{\nabla}(\alpha)_j - t_j \underline{\boldsymbol{u}}_j^n \end{aligned} \tag{17}$$

We assume that it is possible to also write a discrete conservation of momentum across the imaginary control volume C_F in the same form. The resulting equation is:

$$m_F \underline{\boldsymbol{u}}_F^{n+1} = \underline{\tilde{\boldsymbol{u}}}_F - d_F \overline{\nabla}(\alpha P)_F + g_F \overline{\nabla}(\alpha)_F - t_F \underline{\boldsymbol{u}}_F^n \tag{18}$$

Unfortunately, $\underline{\tilde{\boldsymbol{u}}}_F$ is unknown. We therefore assume that interpolating $\underline{\tilde{\boldsymbol{u}}}$ between control volumes $\underline{\tilde{\boldsymbol{u}}}_i$ and $\underline{\tilde{\boldsymbol{u}}}_j$ is a good approximation. It is possible to show, following the approach shown in detail by Bartholomew et al. [24], that the interpolation amounts to Eq. (19). Note that quantities denoted with an overbar $\overline{(\cdot)}_F$ are interpolated at the face between C_i and C_j.

$$\begin{aligned} \underline{\tilde{\boldsymbol{u}}}_F = \overline{m_F u_F^{n+1}} &+ \overline{d_F \overline{\nabla}(\alpha P)_F} - \overline{g_F \overline{\nabla}(\alpha)_F} + \overline{t_F \underline{\boldsymbol{u}}_F} \\ &- d_F \overline{\nabla}(\alpha P)_F + g_F \overline{\nabla}(\alpha)_F - t_F \underline{\boldsymbol{u}}_F \end{aligned} \tag{19}$$

Some assumptions on d_F, m_F, g_F, t_F need to be taken since they are unknown. Therefore:

- Following Bartholomew et al. [24], to ensure that the MWI correction vanishes for a constant or linearly varying pressure gradient we assume $d_i = d_j = d_F$
- Following Bartholomew et al. [24], to ensure that we recover the correct steady state solution we assume $t_F = \overline{t_F}$ and $m_F = \overline{m_F}$
- In addition to Bartholomew et al. [24], to ensure that the MWI correction vanishes for a constant pressure and velocity field we assume $g_F = \overline{g_F}$. More details are given in Appendix B.

Plugging Eq. (19) into the discrete momentum conservation over the imaginary control volume, Eq. (18), we obtain the following MWI face velocity in Eq. (20). The terms d_f, m_F, g_F and t_F can be pulled out of the interpolation operator due to the assumptions we took in the above.

$$\begin{aligned} \underline{\boldsymbol{u}}_F^{MWI} &= \underline{\boldsymbol{u}}_F^{n+1} = \cdots \\ &= \overline{\underline{\boldsymbol{u}}_F^{n+1}} - \frac{d_F}{m_F}\left[\overline{\nabla}(\alpha P)_F - \overline{(\alpha P)_F}\right] + \frac{g_F}{m_F}\left[\overline{\nabla}(\alpha)_F - \overline{\overline{\nabla}(\alpha)_F}\right] - \frac{t_F}{m_F}\left[\underline{\boldsymbol{u}}_F^n - \overline{\underline{\boldsymbol{u}}_F}\right]. \end{aligned} \tag{20}$$

To account for mesh non-orthogonality, we follow the approach proposed by Zhang et al. [32]. Note that $\hat{\boldsymbol{n}}$ and $\hat{\boldsymbol{e}}$ are unit vectors, and $\hat{\boldsymbol{e}} = (\underline{\boldsymbol{x}}_j - \underline{\boldsymbol{x}}_i)/\|\underline{\boldsymbol{x}}_j - \underline{\boldsymbol{x}}_i\|$.

$$\begin{aligned} \underline{\boldsymbol{u}}_F^{MWI} = \overline{\underline{\boldsymbol{u}}_F^{n+1}} &- \frac{d_F}{m_F}\left[\frac{\alpha P_j - \alpha P_i}{\Delta x_{i,j}} - \overline{\overline{\nabla}(\alpha P)_F} \cdot \hat{\boldsymbol{e}}\right]\frac{\hat{\boldsymbol{n}}}{\hat{\boldsymbol{n}} \cdot \hat{\boldsymbol{e}}} \\ &+ \frac{g_F}{m_F}\left[\frac{\alpha_j - \alpha_i}{\Delta x_{i,j}} - \overline{\overline{\nabla}(\alpha)_F} \cdot \hat{\boldsymbol{e}}\right]\frac{\hat{\boldsymbol{n}}}{\hat{\boldsymbol{n}} \cdot \hat{\boldsymbol{e}}} \\ &- \frac{t_F}{m_F}\left[\underline{\boldsymbol{u}}_F^n - \overline{\underline{\boldsymbol{u}}_F}\right] \end{aligned} \tag{21}$$

We use $\underline{\boldsymbol{u}}_F^{MWI}$ to compute the divergence of the velocity in the pressure equation term $\int_{C_i}\left(M_r^2 \alpha c^2 + \kappa\alpha\right)\overline{\nabla}\cdot\underline{\boldsymbol{u}} dV$, instead of using central differences (Green–Gauss). Finally, the divergence is computed as.

$$\overline{\nabla}\cdot\underline{\boldsymbol{u}}\Big|_{C_i} \simeq \frac{1}{|C_i|}\sum_{C_j \in \partial C_i} A_{i,j}\left(\underline{\boldsymbol{u}}_F^{MWI} \cdot \hat{\boldsymbol{n}}\right) \tag{22}$$

We want to stress that the presence of both $\overline{\nabla}(\alpha P)$ and $\overline{\nabla}\alpha$ in the MWI correction is fundamental for preserving the non-disturbance condition as shown in Appendix B. Interpolation on the gradients (e.g. $\overline{\overline{\nabla}(\alpha P)_F}$ in Eq. (21)) can be performed using density weighting, Eq. (23), as proposed by Bartholomew et al. [24] to mitigate oscillations across multi-material interfaces.

$$\overline{f} = \alpha\rho_F\left[I_x \frac{f_i}{\alpha\rho_i} + (1 - I_x)\frac{f_j}{\alpha\rho_j}\right] \quad \textit{where} \quad \frac{1}{\alpha\rho_F} = \frac{I_x}{\alpha\rho_i} + \frac{(1 - I_x)}{\alpha\rho_j} \tag{23}$$

In this work we will use the weighting parameter $I_x = 1/2$ (illustrated in Fig. 2) for simplicity, and also to retain the filtering properties of the MWI on skewed elements at the cost of some accuracy, as proposed in [24]. This negates the previously mentioned density weighting.

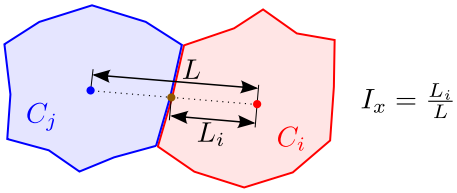

Fig. 2. MWI interpolation factor I_x definition.

3.2. Time discretization

We use a fully implicit time integration scheme to overcome the very stringent acoustic limitation posed by the weakly compressible regime. We briefly describe here the pseudo Newton–Raphson method used in SU2 to advance implicitly in time the unsteady simulation in SU2 [8]. Noting that numerical fluxes are computed at the next time step t^{n+1}.

$$\underline{\boldsymbol{F}}_{i,j}^{cons} + \underline{\boldsymbol{F}}_{i,j}^{non-cons} = \underline{\boldsymbol{F}}_{i,j}^{cons}\left(\underline{\boldsymbol{q}}_i^{n+1}, \underline{\boldsymbol{q}}_j^{n+1}\right) + \underline{\boldsymbol{F}}_{i,j}^{non-cons}\left(\underline{\boldsymbol{q}}_i^{n+1}, \underline{\boldsymbol{q}}_j^{n+1}\right) \tag{24}$$

The solution at time $(\cdot)^{n+1}$ is iteratively $(k \rightarrow k+1)$ computed solving the linear system. The Jacobian's $[i,j]$ element denoted as $J_{[i,j]}$ is defined in Eq. (25) together with the implicit solution method.

$$J_{[i,j]}(k) = \frac{\partial R_{[i]}^{n+1}}{\partial q_{[j]}}(k) \quad \rightarrow \quad \begin{cases} \underline{\underline{\boldsymbol{J}}}(k)\Delta\underline{\boldsymbol{q}}^{n+1}(k) = -\underline{\boldsymbol{R}}^{n+1}(k) & \textit{linear system solution} \\ \underline{\boldsymbol{q}}^{n+1}(k+1) = \underline{\boldsymbol{q}}^{n+1}(k) + \Delta\underline{\boldsymbol{q}}^{n+1}(k) & \textit{solution update} \end{cases} \tag{25}$$

4. Results

In this section four numerical tests will be shown. First, in Section 4.1 we will show that the non disturbance condition is met in a volume fraction advection test. Second, in Section 4.2 we will evaluate convergence to the entropic solution and no spurious mixing in a shock tube. Third, in Section 4.3 the effect of MWI will be assessed on a newly devised slip bubble test case mimicking the flow over a cylinder in a two-phase flow setting. Lastly, in Section 4.4 we will try to match well known experimental visualizations of a helium bubble interacting with an air shock. This last test case is a compressible one, therefore outside the main scope of the scheme, but it has been added to show how the model is also able to satisfactorily capture the physics of flows with $M > 1$.

The present numerical approach suffers from an issue when the volume fraction tends to zero and we have sharp gradients as in the case of an interface between pure fluids. When the volume fraction of a phase goes to zero, solving for that phase's pressure loses physical meaning. If we position ourselves across a pure fluid interface ($\overline{\nabla}\alpha_k \gg 1$), the time discrete pressure equation from Eq. (5) for the fluid with very small volume fraction ($\alpha_k \ll 1$) shows the following:

$$\underbrace{M_r^2\alpha_k\left(\frac{P_k^{n+1}-P_k^n}{\Delta t} + \underline{\boldsymbol{u}}_k \cdot \overline{\nabla}P_k\right)}_{\propto\alpha_k\ll 1} + \underbrace{\left(M_r^2\alpha_k\rho_k c_k^2 + \kappa_k\alpha_k\right)\overline{\nabla}\cdot\underline{\boldsymbol{u}}_k}_{\propto\alpha_k\ll 1} - \underbrace{\left(M_r^2\rho_k c_{l,k}^2 + \kappa_k\right)\left(\underline{\boldsymbol{u}}_l - \underline{\boldsymbol{u}}_k\right)\cdot\overline{\nabla}\alpha_k}_{\propto\overline{\nabla}\alpha_k\gg 1} = 0 \tag{26}$$

A numerical update of the pressure may lead to a negative pressure due to a division by α_k. This is a well documented problem that prevents us from treating low volume fractions, see for example Saurel & Abgrall [33], Abgrall & Saurel [34]. In more conventional approaches this is sometimes circumvented by changing the numerical approach when the volume fraction goes below a certain threshold. This is an area where further work is needed.

4.1. Volume fraction advection - Non disturbance condition

This simple test consists in the advection of a circular area with a higher content of water centered in $x = 0.3$ m and surrounded by a flow of air, at pressure and velocity equilibrium. For simplicity we will refer to it as a droplet, even if the volume fraction is not $\simeq 1$. Exploiting the symmetry of the problem, the domain, sketched in Fig. 3, represents only half of the tube. The corresponding triangular mesh is reported in Fig. 4. The initial flow conditions, along with the information about the discretization and the thermodynamic data, are given in Table 1. The goal of this test is twofold: check that the droplet interface is advected correctly and that the non-disturbance condition is satisfied, namely that the velocity and pressure remain constant.

In Fig. 5(c) we compare results obtained using $CFL(|u|+c) = 10$ and $h = 0.005$ m (which corresponds to $n_x = 200$ elements in 1D) with 1D results from Re & Abgrall [1] obtained using a finer mesh with $n_x = 400$ elements and $CFL(|u|) = 0.5$. This comparison is not meant to be quantitative as the numerical settings are different. The volume fraction plots compare well although the 1D results have been obtained with a larger time step than the 2D ones. The droplet is advected at the correct speed of 100 m/s, although some smearing of the interface can be noticed in Fig. 5(c), due to the use of a first-order scheme over a coarse mesh. The pressure and velocity profile, shown in Figs. 5(b) and 5(a), respectively, do not present any oscillations, confirming that the non-disturbance condition is preserved.

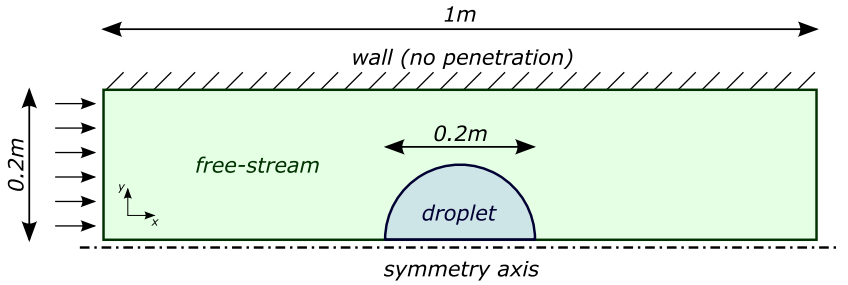

Fig. 3. Volume fraction advection domain definition.

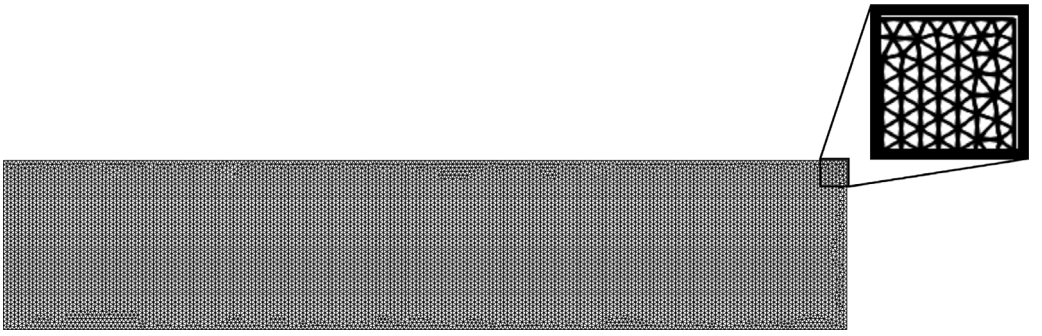

Fig. 4. Volume fraction advection mesh with triangular elements of typical mesh size $h = \frac{1}{200}\frac{[m]}{[elements\ x]} = 0.005$ m.

Table 1
Numerical setup for volume fraction advection test.

Numerics	$CFL(\lvert u\rvert + c) = 10$	
Mesh	$h = \frac{1}{200}\frac{[m]}{[elements\ x]} = 0.005$ m	*triangular*
I.C. *Droplet*	$\alpha_{air} = 0.1$ $\rho_{air} = 1$ kg/m^3 $P_{air} = 10^6$ Pa $\underline{\boldsymbol{u}}_{air} = \begin{bmatrix}100 & 0\end{bmatrix}$ m/s	$\alpha_{H_2O} = 0.9$ $\rho_{H_2O} = 1000$ kg/m^3 $P_{H_2O} = 10^6$ Pa $\underline{\boldsymbol{u}}_{H_2O} = \begin{bmatrix}100 & 0\end{bmatrix}$ m/s
I.C. *Free-Stream*	$\alpha_{air} = 0.9$ $\rho_{air} = 1$ kg/m^3 $P_{air} = 10^6$ Pa $\underline{\boldsymbol{u}}_{air} = \begin{bmatrix}100 & 0\end{bmatrix}$ m/s	$\alpha_{H_2O} = 0.1$ $\rho_{H_2O} = 1000$ kg/m^3 $P_{H_2O} = 10^6$ Pa $\underline{\boldsymbol{u}}_{H_2O} = \begin{bmatrix}100 & 0\end{bmatrix}$ m/s
Thermodynamics	$\gamma_{air} = 1.4$ $c_{v,air} = 717.60$ J/kg K $q_{\infty,air} = 0$ J/kg $P_{\infty,air} = 0$ Pa	$\gamma_{H_2O} = 4.4$ $c_{v,H_2O} = 4178$ J/kg K $q_{\infty,H_2O} = 0$ J/kg $P_{\infty,H_2O} = 6 \cdot 10^8$ Pa

4.2. No mixing shock tube - Entropic solution convergence

The goal of this test is to assess mesh convergence to the entropic solution of a shock tube with a jump of pressure and temperature at $x = 0$ m and everything initially at rest. The domain is sketched in Fig. 6. The tube is filled with water and air, both with $\alpha = 0.5$. The two phases are supposed to not mix since we are only considering the hyperbolic part of the Baer–Nunziato equations. Both phases should evolve following their separate pure fluid analytic solution of the Euler equations. Initial conditions, mesh and time discretization data, and the thermodynamic properties of the fluids are given in Table 2. Results for this test case have been obtained on uniform orthogonal meshes with quadrilateral elements.

Results in Fig. 7 show great agreement with the exact solution for the finest mesh with $n_x = 3200$. Wave speed are caught accurately for both phases. The volume fraction in Fig. 7(a) remains constant, and phases do not mix.

We can compute a measure of the error as Eq. (27). The resulting plots show convergence towards the entropic solution both with spatial refinement in Fig. 9 and with time step refinement in Fig. 8. We do not aim to measure the rate of

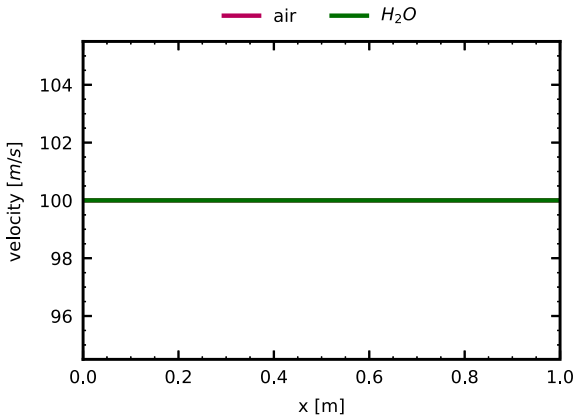

(a) Velocity

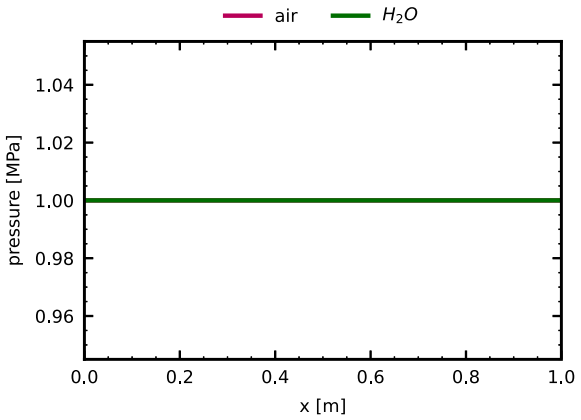

(b) Pressure

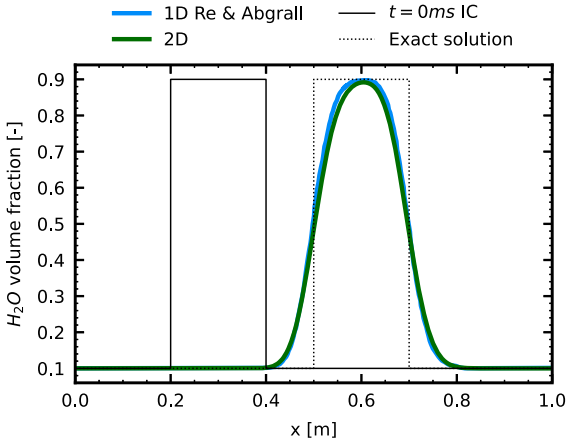

(c) Volume fraction

Fig. 5. Droplet advection results at $t = 3$ ms at the symmetry axis with $CFL(|u|+c) = 10$ and $h = 0.005$ m (which corresponds to $n_x = 200$ elements in 1D) compared to Re & Abgrall [1] 1D results with $n_x = 400$ elements and $CFL(|u|) = 0.5$.

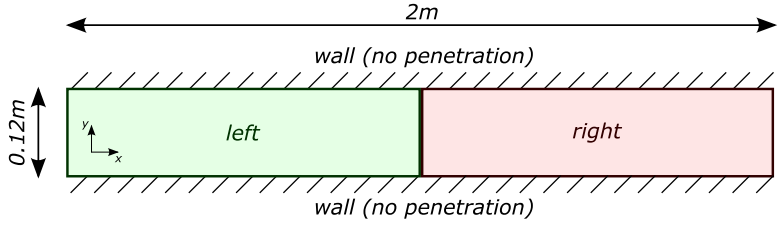

Fig. 6. No mixing shock tube domain definitions.

Table 2
Numerical setup for no mixing shock tube test.

Mesh	*regular quadrilateral*	
Mesh convergence	$\frac{n_x}{n_y} = \frac{50}{3}, \frac{100}{6}, \frac{200}{12}, \frac{400}{24}, \frac{800}{48}, \frac{1600}{96}, \frac{3200}{192}$	$CFL(\lvert\underline{\boldsymbol{u}}\rvert + c) = 1$
Time convergence	$\frac{n_x}{n_y} = \frac{400}{24}$	$CFL(\lvert\underline{\boldsymbol{u}}\rvert + c) = 1, 2, 4, 8, 16$
I.C. *Left*	$\alpha_{air} = 0.5$ $\rho_{air} = 129$ kg/m^3 $P_{air} = 10^7$ Pa $\underline{\boldsymbol{u}}_{air} = \begin{bmatrix}0 & 0\end{bmatrix}$ m/s	$\alpha_{H_2O} = 0.5$ $\rho_{H_2O} = 159$ kg/m^3 $P_{H_2O} = 10^7$ Pa $\underline{\boldsymbol{u}}_{H_2O} = \begin{bmatrix}0 & 0\end{bmatrix}$ m/s
I.C. *Right*	$\alpha_{air} = 0.5$ $\rho_{air} = 64.5$ kg/m^3 $P_{air} = 5 \cdot 10^6$ Pa $\underline{\boldsymbol{u}}_{air} = \begin{bmatrix}0 & 0\end{bmatrix}$ m/s	$\alpha_{H_2O} = 0.5$ $\rho_{H_2O} = 157.7$ kg/m^3 $P_{H_2O} = 5 \cdot 10^6$ Pa $\underline{\boldsymbol{u}}_{H_2O} = \begin{bmatrix}0 & 0\end{bmatrix}$ m/s
Thermodynamics	$\gamma_{air} = 1.4$ $c_{v,air} = 717.60$ J/kg K $q_{\infty,air} = 0$ J/kg $P_{\infty,air} = 0$ Pa	$\gamma_{H_2O} = 4.4$ $c_{v,H_2O} = 4178$ J/kg K $q_{\infty,H_2O} = 0$ J/kg $P_{\infty,H_2O} = 6 \cdot 10^8$ Pa

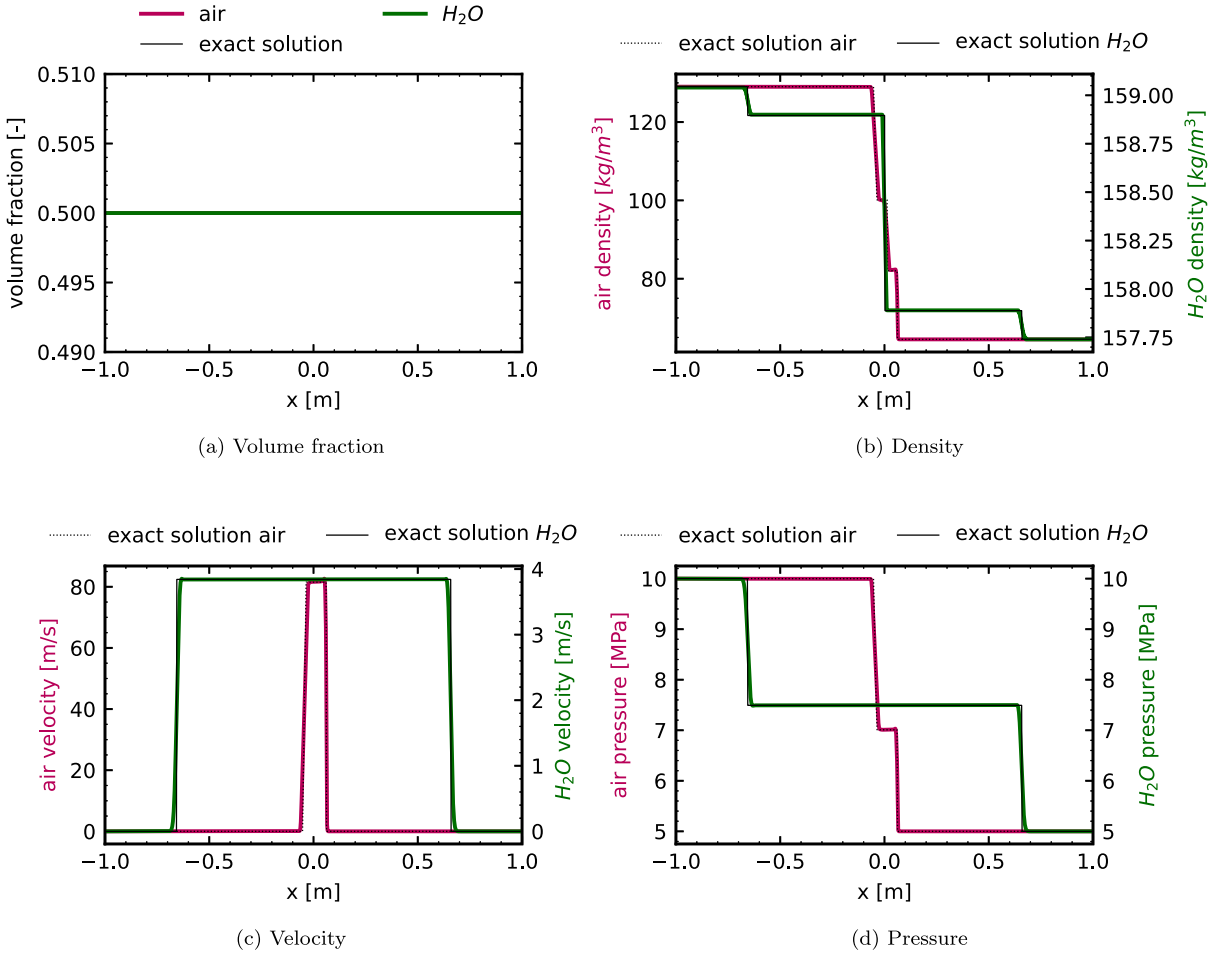

(a) Volume fraction

(b) Density

(c) Velocity

(d) Pressure

Fig. 7. No mixing shock results at $t = 0.16$ ms compared to the analytic solution for each phase for $n_x = 3200$ with $CFL(\lvert\underline{\boldsymbol{u}}\rvert + c) = 1$.

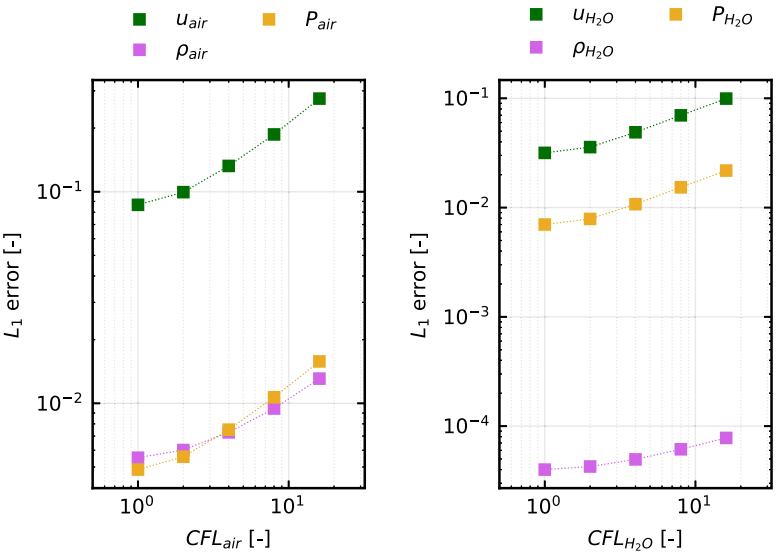

(a) Air (b) H_2O

Fig. 8. No mixing shock L_1 error for time convergence with $n_x = 400$.

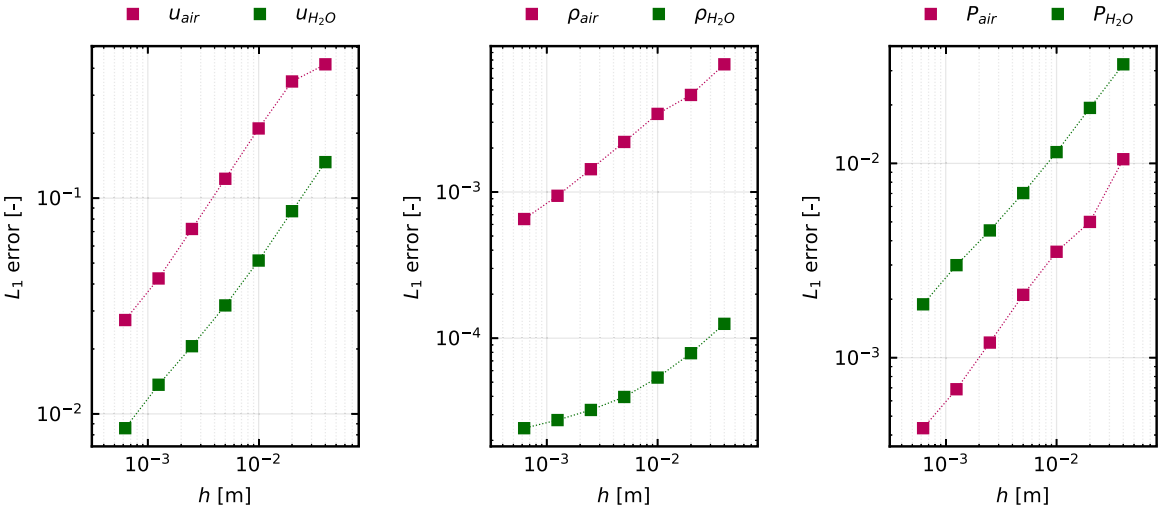

(a) Velocity (b) Density (c) Pressure

Fig. 9. No mixing shock L_1 error for mesh convergence with $CFL(|\underline{\boldsymbol{u}}| + c) = 1$.

convergence but only show convergence to the entropic solution.

$$L_1\ error(t) = \frac{\int_\Omega |f_{numeric}(t) - f_{exact}(t)| d\Omega}{\int_\Omega |f_{exact}(t)| d\Omega} \tag{27}$$

4.3. Low Mach Helium slip-bubble - Pressure checkerboarding

This case has been devised to test pressure checkerboarding, with and without MWI, in a weakly compressible setting. It is supposed to mimic the flow over a cylinder, which is the trademark 2D incompressible test case. It consists of an air bubble moving 20% slower than the Helium around it ($M_{\text{He}} \simeq 0.05$). See Fig. 10 for a domain sketch and Table 3 for the setup data.

We use two different meshes, Fig. 11, with the same typical mesh size $h = 0.0053$ m to showcase how a more regular mesh exhibits a much bigger amount of pressure checkerboarding.

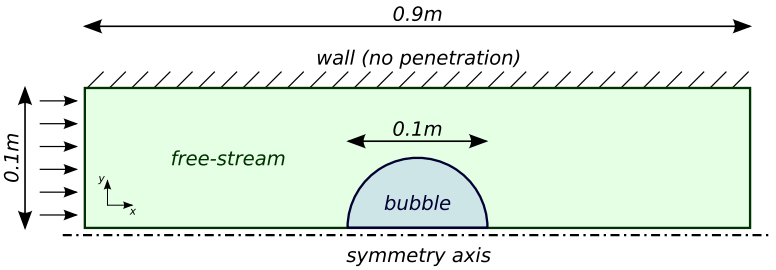

Fig. 10. Low Mach Helium slip-bubble domain definitions.

Table 3
Numerical setup for low Mach Helium slip-bubble test.

Numerics	$CFL(\lvert\underline{\boldsymbol{u}}\rvert + c) = 0.1$	
Mesh	$h = 0.0053$ m *triangular*	
I.C. *Bubble*	$\alpha_{air} = 0.6$ $\rho_{air} = 1$ kg/m^3 $P_{air} = 101\,325$ Pa $\underline{\boldsymbol{u}}_{air} = \begin{bmatrix}34.719 & 0\end{bmatrix}$ m/s	$\alpha_{\mathrm{He}} = 0.4$ $\rho_{\mathrm{He}} = 0.1626$ kg/m^3 $P_{\mathrm{He}} = 101\,325$ Pa $\underline{\boldsymbol{u}}_{\mathrm{He}} = \begin{bmatrix}34.719 & 0\end{bmatrix}$ m/s
I.C. *Free-Stream*	$\alpha_{air} = 0.6$ $\rho_{air} = 1$ kg/m^3 $P_{air} = 101\,325$ Pa $\underline{\boldsymbol{u}}_{air} = \begin{bmatrix}45 & 0\end{bmatrix}$ m/s	$\alpha_{\mathrm{He}} = 0.4$ $\rho_{\mathrm{He}} = 0.1626$ kg/m^3 $P_{\mathrm{He}} = 101\,325$ Pa $\underline{\boldsymbol{u}}_{\mathrm{He}} = \begin{bmatrix}45 & 0\end{bmatrix}$ m/s
Thermodynamics	$\gamma_{air} = 1.4$ $c_{v,air} = 717.60$ J/kg K $q_{\infty,air} = 0$ J/kg $P_{\infty,air} = 0$ Pa	$\gamma_{\mathrm{He}} = 1.667$ $c_{v,\mathrm{He}} = 3115.6$ J/kg K $q_{\infty,\mathrm{He}} = 0$ J/kg $P_{\infty,\mathrm{He}} = 0$ Pa

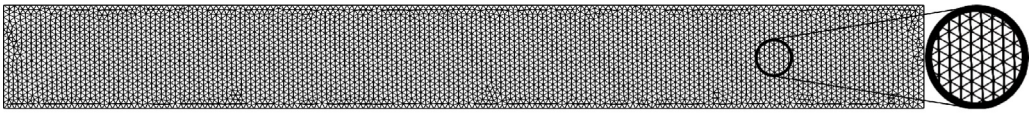

(a) Regular mesh

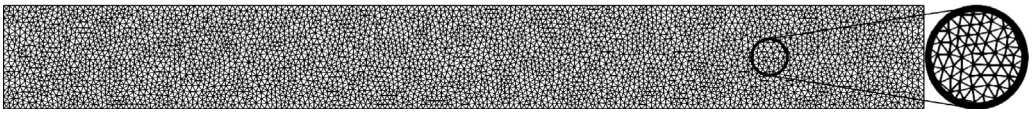

(b) Irregular mesh

Fig. 11. Meshes for the low Mach Helium slip-bubble.

The results of Fig. 12(a) obtained on mesh Fig. 11(a) show a great deal more checkerboarding than the results of Fig. 13(a) obtained on mesh Fig. 11(b). The use of MWI (Figs. 12(b) 13(b)) can decrease the amount of checkerboarding, but cannot prevent it completely as staggering would. The dampening of pressure oscillations occurs at the cost of some additional numerical dissipation on the pressure field, with the pressure waves arising from the velocity difference between the bubble and the free-stream being slightly more smeared with MWI.

MWI does cure checkerboarding almost completely in the irregular mesh Fig. 15(b), while the regular mesh Fig. 14(b) still exhibits some, although reduced.

4.4. Helium bubble shock interaction - Experimental data matching

Finally, to put everything together we show here a test recreating an experiment from [35]. An initially stationary Helium bubble is impacted by an air shock at $M = 1.22$ at time $t = 0$ μs, after 36 μs from the start of the simulation. The goal is to match the position and overall shape of the bubble using the schlieren imagery from [35]. See Fig. 16 for a sketch of the domain and Table 4 for the setup data.

As Fig. 17 shows in two separate time steps ($t = 427$ μs and $t = 674$ μs after the shock reaches the bubble's leading edge), the bubble shape and position is overall well caught. Considering this solver is aimed at weakly compressible cases

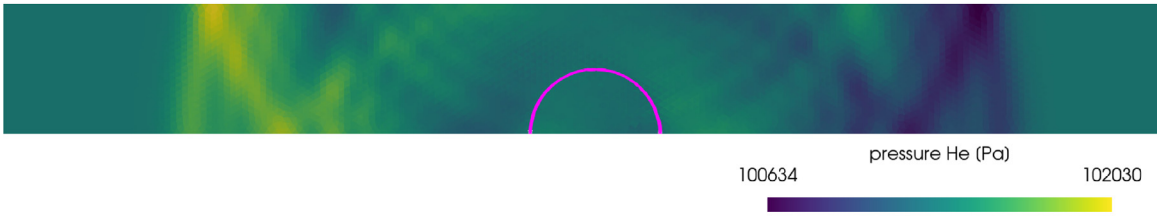

(a) No MWI

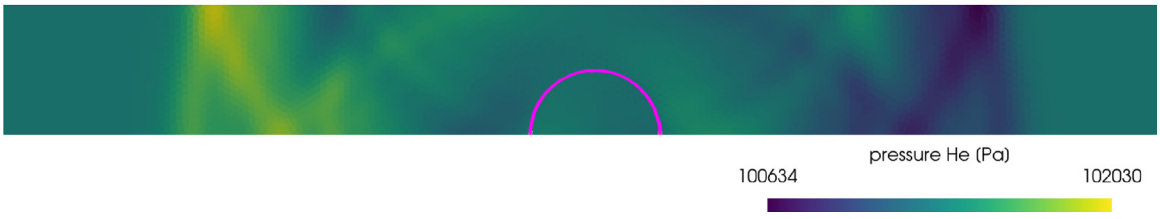

(b) With MWI

Fig. 12. Low Mach Helium slip-bubble pressure, pressure field at $t = 0.3$ ms for the regular mesh.

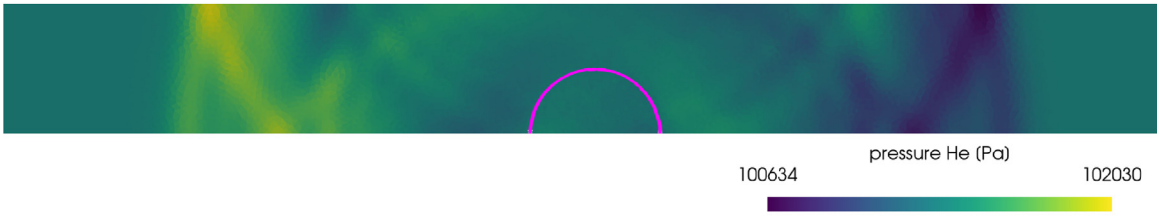

(a) No MWI

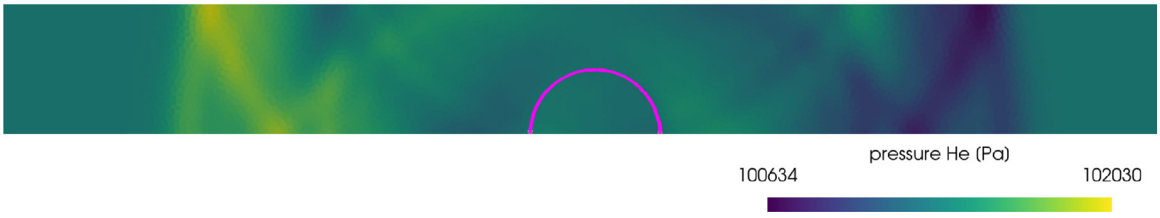

(b) MWI

Fig. 13. Low Mach Helium slip-bubble pressure, pressure field at $t = 0.3$ ms for the irregular mesh.

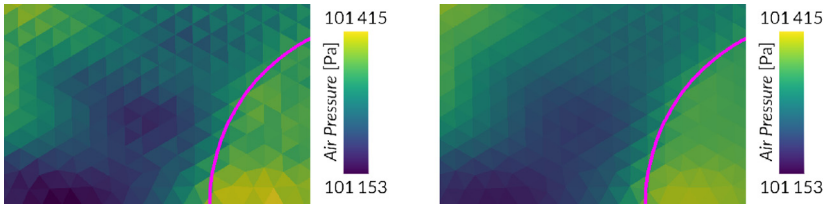

(a) No MWI (b) MWI

Fig. 14. Low Mach Helium slip-bubble pressure, pressure field at $t = 0.3$ ms for the regular mesh.

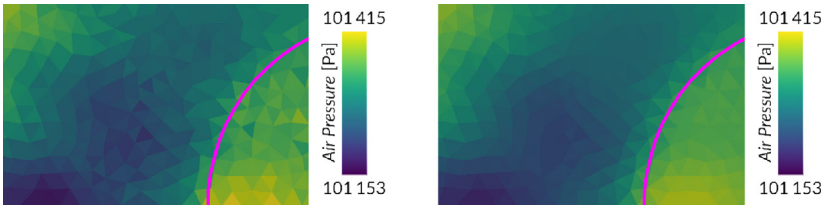

(a) No MWI (b) MWI

Fig. 15. Low Mach Helium slip-bubble pressure, pressure field at $t = 0.3$ ms for the irregular mesh.

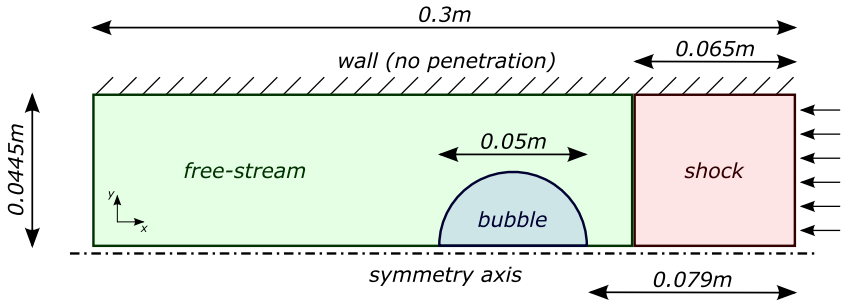

Fig. 16. Helium bubble shock interaction domain definitions.

Table 4
Numerical setup for Helium bubble shock interaction test from [35].

Numerics	$\Delta t = 0.1$ μs	$\Delta t = 6$ μs
Meshes	$n_x = 250$	*quadrilateral*
I.C. *Bubble*	$\alpha_{air} = 0.07$ $\rho_{air} = 1.4$ kg/m^3 $P_{air} = 100\,000$ Pa $\underline{\boldsymbol{u}}_{air} = \begin{bmatrix} 0 & 0 \end{bmatrix}$ m/s	$\alpha_{\mathrm{He}} = 0.93$ $\rho_{\mathrm{He}} = 0.2546$ kg/m^3 $P_{\mathrm{He}} = 100\,000$ Pa $\underline{\boldsymbol{u}}_{\mathrm{He}} = \begin{bmatrix} 0 & 0 \end{bmatrix}$ m/s
I.C. *Shock*	$\alpha_{air} = 0.93$ $\rho_{air} = 1.92691$ kg/m^3 $P_{air} = 156\,980$ Pa $\underline{\boldsymbol{u}}_{air} = \begin{bmatrix} -104.42 & 0 \end{bmatrix}$ m/s	$\alpha_{\mathrm{He}} = 0.07$ $\rho_{\mathrm{He}} = 0.2546$ kg/m^3 $P_{\mathrm{He}} = 100\,000$ Pa $\underline{\boldsymbol{u}}_{\mathrm{He}} = \begin{bmatrix} 0 & 0 \end{bmatrix}$ m/s
I.C. *Free-Stream*	$\alpha_{air} = 0.93$ $\rho_{air} = 1.4$ kg/m^3 $P_{air} = 100\,000$ Pa $\underline{\boldsymbol{u}}_{air} = \begin{bmatrix} 0 & 0 \end{bmatrix}$ m/s	$\alpha_{\mathrm{He}} = 0.07$ $\rho_{\mathrm{He}} = 0.2546$ kg/m^3 $P_{\mathrm{He}} = 100\,000$ Pa $\underline{\boldsymbol{u}}_{\mathrm{He}} = \begin{bmatrix} 0 & 0 \end{bmatrix}$ m/s
Thermodynamics	$\gamma_{air} = 1.4$ $c_{v,air} = 717.60$ J/kg K $q_{\infty,air} = 0$ J/kg $P_{\infty,air} = 0$ Pa	$\gamma_{\mathrm{He}} = 1.667$ $c_{v,\mathrm{He}} = 3115.6$ J/kg K $q_{\infty,\mathrm{He}} = 0$ J/kg $P_{\infty,\mathrm{He}} = 0$ Pa

and that the Baer–Nunziato equations are derived through an ensemble average, and therefore they describe the flow in a statistical repeatability sense, the agreement with experimental data is more than satisfactory. Furthermore, an increase in time step has negligible effects on the prediction of the bubble position, with some expected smearing of the interface. Although the mesh is not fine enough to resolve the bubble core's topology, results compare well with the ones presented by Daude et al. [36] using HLL and HLLC. The bubble's trailing edge in Fig. 17(a) is not perfectly aligned with experimental data. This could be due to the non-conservative scheme in use not being able to accurately predict shock speeds.

5. Conclusions

In this paper a set of strategies to simulate weakly compressible two phase flows on unstructured meshes is presented. In particular, a novel formulation of the Momentum Weighted Interpolation (Rhie-Chow) has been derived for the Baer–Nunziato equations. The proposed approach has been thoroughly tested against analytic results and experimental data. The convergence rate (both in time and space) has been approximately evaluated in a worst case scenario with discontinuities.

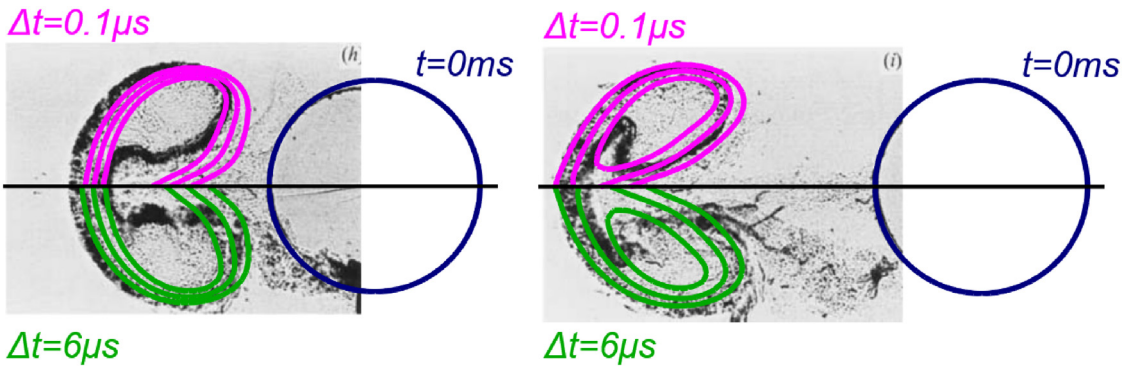

(a) $t = 427\mu s$ after first shock-bubble interaction (b) $t = 674\mu s$ after first shock-bubble interaction

Fig. 17. Helium bubble shock interaction, experimental visualization comparison [35]. Numerical bubble contours of the volume fraction for $\alpha = [0.4, 0.5, 0.6]$ are overimpressed for $\Delta t = 0.1$ μs in pink, and $\Delta t = 6$ μs in green. In blue the $t = 0$ ms bubble initial position.

The fully implicit formulation allows the use of high *CFL* numbers. The effectiveness of the Momentum Weighted Interpolation has been assessed on a purpose built test case, showcasing a great reduction in pressure checkerboarding. As a final test, an experimental visualization of a shock-bubble interaction has been simulated showing good agreement also with real world behavior.

Data availability

The authors are unable or have chosen not to specify which data has been used.

Acknowledgments

Rémi Abgrall is partially funded by SNF, Switzerland Grant 200020_204917. Giuseppe Sirianni was partially funded by Rémi Abgrall's UZH Einrichtungkredit, Switzerland.

Appendix A. Momentum phase coupling term derivation

The discretization of the momentum phase coupling term must preserve the non-disturbance condition. To derive it we start by writing the discrete mass and momentum equations for the ith control volume $(\cdot)_i$:

$$\begin{aligned}
&|C_i|\frac{\alpha\rho_i^{n+1}-\alpha\rho_i^n}{\Delta t} && + \sum_{C_j\in\partial C_i} A_{i,j}\left[\frac{1}{2}\left(\alpha\rho\underline{\boldsymbol{u}}_i\cdot\hat{\boldsymbol{n}}_{i,j}+\alpha\rho\underline{\boldsymbol{u}}_j\cdot\hat{\boldsymbol{n}}_{i,j}\right)-\frac{1}{2}\lambda_{\alpha\rho}\left(\alpha\rho_j-\alpha\rho_i\right)\right]=0\\
&|C_i|\frac{\alpha\rho\underline{\boldsymbol{u}}_i^{n+1}-\alpha\rho\underline{\boldsymbol{u}}_i^n}{\Delta t} && + \sum_{C_j\in\partial C_i} A_{i,j}\left[\frac{1}{2}\left(\alpha\rho\underline{\boldsymbol{u}}_i\underline{\boldsymbol{u}}_i\cdot\hat{\boldsymbol{n}}_{i,j}+\alpha_i P_i\hat{\boldsymbol{n}}_{i,j}+\alpha\rho\underline{\boldsymbol{u}}_j\underline{\boldsymbol{u}}_j\cdot\hat{\boldsymbol{n}}_{i,j}+\alpha_j P_j\hat{\boldsymbol{n}}_{i,j}\right)\right.\\
& && \left.-\frac{1}{2}\lambda_{\alpha\rho\underline{\boldsymbol{u}}}\left(\alpha\rho\underline{\boldsymbol{u}}_j-\alpha\rho\underline{\boldsymbol{u}}_i\right)\right]-\underline{\underline{\boldsymbol{NC}}}_{P_i\overline{\nabla}\alpha}=\underline{\boldsymbol{0}}\,.
\end{aligned}\tag{A.1}$$

We now assume that $\underline{\boldsymbol{u}}$ and P are constant in space and that the discretization of the non-conservative momentum coupling term $\underline{\underline{\boldsymbol{NC}}}_{P_i\overline{\nabla}\alpha}$ does not affect this, and therefore $\underline{\boldsymbol{u}}$ and P remain constant in time too:

$$\begin{aligned}
&|C_i|\frac{\alpha\rho_i^{n+1}-\alpha\rho_i^n}{\Delta t} && + \sum_{C_j\in\partial C_i} A_{i,j}\left[\frac{1}{2}\left(\alpha\rho_i+\alpha\rho_j\right)\left(\underline{\boldsymbol{u}}\cdot\hat{\boldsymbol{n}}_{i,j}\right)-\frac{1}{2}\lambda_{\alpha\rho}\left(\alpha\rho_j-\alpha\rho_i\right)\right]=0\\
&|C_i|\frac{\alpha\rho_i^{n+1}-\alpha\rho_i^n}{\Delta t}\underline{\boldsymbol{u}} && + \sum_{C_j\in\partial C_i} A_{i,j}\left\{\left[\frac{1}{2}\left(\alpha\rho_i+\alpha\rho_j\right)\underline{\boldsymbol{u}}\left(\underline{\boldsymbol{u}}\cdot\hat{\boldsymbol{n}}_{i,j}\right)+\frac{1}{2}\left(\alpha_i+\alpha_j\right)P\hat{\boldsymbol{n}}_{i,j}\right]\right.\\
& && \left.-\frac{1}{2}\lambda_{\alpha\rho\underline{\boldsymbol{u}}}\left(\alpha\rho_j-\alpha\rho_i\right)\underline{\boldsymbol{u}}\right\}-\underline{\underline{\boldsymbol{NC}}}_{P_i\overline{\nabla}\alpha}=\underline{\boldsymbol{0}}
\end{aligned}\tag{A.2}$$

If we now assume that $\lambda_{\alpha\rho} = \lambda_{\alpha\rho\underline{\boldsymbol{u}}}$, therefore we use the same wave speed for both mass and momentum convective fluxes, we can substitute the mass equation into the momentum equation.

$$
\begin{aligned}
&- \sum_{C_j \in \partial C_i} A_{i,j} \left[\frac{1}{2} \left(\alpha\rho_i + \alpha\rho_j \right) \underline{\boldsymbol{u}} \left(\underline{\boldsymbol{u}} \cdot \hat{\boldsymbol{n}}_{i,j} \right) - \frac{1}{2} \lambda_{\alpha\rho} \left(\alpha\rho_j - \alpha\rho_i \right) \underline{\boldsymbol{u}} \right] \\
&+ \sum_{C_j \in \partial C_i} A_{i,j} \left\{ \left[\frac{1}{2} \left(\alpha\rho_i + \alpha\rho_j \right) \underline{\boldsymbol{u}} \left(\underline{\boldsymbol{u}} \cdot \hat{\boldsymbol{n}}_{i,j} \right) + \frac{1}{2} \left(\alpha_i + \alpha_j \right) P \hat{\boldsymbol{n}}_{i,j} \right] \right. \\
&\left. - \frac{1}{2} \lambda_{\alpha\rho\underline{\boldsymbol{u}}} \left(\alpha\rho_j - \alpha\rho_i \right) \underline{\boldsymbol{u}} \right\} - \underline{\underline{\boldsymbol{NC}}}_{P_I \overline{\nabla} \alpha} = \underline{\boldsymbol{0}}
\end{aligned}
\tag{A.3}
$$

For a constant pressure field the interface pressure P_I is

$$
P_I = \sum_{i}^{N_{phases}} \alpha_i P_i = \left(\sum_{i}^{N_{phases}} \alpha_i \right) P = 1 \, P = P \, . \tag{A.4}
$$

Therefore a valid choice for the discretization of the momentum non-conservative phase-coupling term is

$$
-\underline{\underline{\boldsymbol{NC}}}_{P_I \overline{\nabla} \alpha} = - \sum_{C_j \in \partial C_i} A_{i,j} \left[\frac{1}{2} \left(\alpha_i + \alpha_j \right) P_I \hat{\boldsymbol{n}}_{i,j} \right] . \tag{A.5}
$$

Appendix B. Momentum Weighted Interpolation and the non disturbance condition

In this section, we show that the MWI correction is identically zero when pressure and velocity are constant under the assumption that $g_F = \overline{g_F}$, therefore it does not affect the non-disturbance condition. Let us assume $\underline{\boldsymbol{u}}$ and P constant in space and time, and rewrite Eq. (21) with this assumption in Eq. (B.1).

$$
\begin{aligned}
\underline{\boldsymbol{u}}_F^{MWI} = \underline{\boldsymbol{u}} \quad & - \frac{d_F}{m_F} \left[\frac{\alpha_j - \alpha_i}{\Delta x_{i,j}} - \overline{\overline{\nabla}(\alpha)} \cdot \hat{\boldsymbol{e}} \right] \frac{\hat{\boldsymbol{n}}}{\hat{\boldsymbol{n}} \cdot \hat{\boldsymbol{e}}} \cdot (P) \\
& + \frac{g_F}{m_F} \left[\frac{\alpha_j - \alpha_i}{\Delta x_{i,j}} - \overline{\overline{\nabla}(\alpha)} \cdot \hat{\boldsymbol{e}} \right] \frac{\hat{\boldsymbol{n}}}{\hat{\boldsymbol{n}} \cdot \hat{\boldsymbol{e}}} \\
& - \frac{t_F}{m_F} \left[\underline{\boldsymbol{u}} - \underline{\boldsymbol{u}} \right]
\end{aligned}
\tag{B.1}
$$

Note that $g = dP_I$ but $P_I = P$ under the constant pressure assumption, therefore $g_F = d_F P$.

$$
\begin{aligned}
\underline{\boldsymbol{u}}_F^{MWI} = \underline{\boldsymbol{u}} \quad & - \frac{d_F}{m_F} \left[\frac{\alpha_j - \alpha_i}{\Delta x_{i,j}} - \overline{\overline{\nabla}(\alpha)} \cdot \hat{\boldsymbol{e}} \right] \frac{\hat{\boldsymbol{n}}}{\hat{\boldsymbol{n}} \cdot \hat{\boldsymbol{e}}} \cdot (P) \\
& + \frac{d_F}{m_F} \left[\frac{\alpha_j - \alpha_i}{\Delta x_{i,j}} - \overline{\overline{\nabla}(\alpha)} \cdot \hat{\boldsymbol{e}} \right] \frac{\hat{\boldsymbol{n}}}{\hat{\boldsymbol{n}} \cdot \hat{\boldsymbol{e}}} \cdot (P)
\end{aligned}
\tag{B.2}
$$

Since $\underline{\boldsymbol{u}}$ is constant, $\overline{\nabla} \cdot \underline{\boldsymbol{u}}$ is identically zero, and pressure is not disturbed by the MWI.

References

[1] B. Re, R. Abgrall, A pressure-based method for weakly compressible two-phase flows under a baer–nunziato type model with generic equations of state and pressure and velocity disequilibrium, International Journal for Numerical Methods in Fluids (ISSN: 0271-2091) 94 (2022) 1183–1232, http://dx.doi.org/10.1002/fld.5087.

[2] M. Baer, J. Nunziato, A two-phase mixture theory for the deflagration-to-detonation transition (ddt) in reactive granular materials, Int. J. Multiph. Flow. 12 (6) (1986) 861–889, http://dx.doi.org/10.1016/0301-9322(86)90033-9, URL https://www.sciencedirect.com/science/article/pii/0301932286900339.

[3] U. Singh, Carbon capture and storage: An effective way to mitigate global warming, Current Sci. 105 (2013) 914–922.

[4] S.T. Munkejord, M. Hammer, S.W. Løvseth, CO2 transport: Data and models – A review, Appl. Energy 169 (2016) 499–523, http://dx.doi.org/10.1016/j.apenergy.2016.01.100, URL https://www.sciencedirect.com/science/article/pii/S0306261916300885.

[5] F. Denner, C.-N. Xiao, B.G. van Wachem, Pressure-based algorithm for compressible interfacial flows with acoustically-conservative interface discretisation, J. Comput. Phys. 367 (2018) 192–234, http://dx.doi.org/10.1016/j.jcp.2018.04.028, URL https://www.sciencedirect.com/science/article/pii/S0021999118302535.

[6] B. Duret, R. Canu, J. Reveillon, F. Demoulin, A pressure based method for vaporizing compressible two-phase flows with interface capturing approach, Int. J. Multiph. Flow. 108 (2018) 42–50, http://dx.doi.org/10.1016/j.ijmultiphaseflow.2018.06.022, URL https://www.sciencedirect.com/science/article/pii/S0301932218302799.

[7] R. Abgrall, P. Bacigaluppi, S. Tokareva, A high-order nonconservative approach for hyperbolic equations in fluid dynamics, Comput. & Fluids 169 (2018) 10–22, http://dx.doi.org/10.1016/j.compfluid.2017.08.019, URL https://www.sciencedirect.com/science/article/pii/S0045793017302906, Recent progress in nonlinear numerical methods for time-dependent flow & transport problems.
[8] T. Economon, F. Palacios, S. Copeland, T. Lukaczyk, J. Alonso, SU2: An open-source suite for multiphysics simulation and design, AIAA J. 54 (2015) 1–19, http://dx.doi.org/10.2514/1.J053813.
[9] A. Date, Fluid dynamical view of pressure checkerboarding problem and smoothing pressure correction on meshes with colocated variables, Int. J. Heat Mass Transfer 46 (2003) http://dx.doi.org/10.1016/S0017-9310(03)00332-6.
[10] D.A. Kopriva, A staggered-grid multidomain spectral method for the compressible Navier–Stokes equations, J. Comput. Phys. 143 (1) (1998) 125–158.
[11] H. Meier, J. Alves, M. Mori, Comparison between staggered and collocated grids in the finite-volume method performance for single and multi-phase flows, Comput. Chem. Eng. 23 (3) (1999) 247–262, http://dx.doi.org/10.1016/S0098-1354(98)00270-1, URL https://www.sciencedirect.com/science/article/pii/S0098135498002701.
[12] I. Wenneker, G. Segal, P. Wesseling, An unstructured staggered scheme for the Navier—Stokes equations, in: F. Brezzi, A. Buffa, S. Corsaro, A. Murli (Eds.), Numerical Mathematics and Advanced Applications, Springer Milan, Milano, 2003, pp. 189–197.
[13] B. LV, S. JIN, C. fang A.I., A conservative unstructured staggered grid scheme for incompressible Navier-Stokes equations, J. Hydrodynamics, Ser. B 22 (2) (2010) 173–184, http://dx.doi.org/10.1016/S1001-6058(09)60043-3, URL https://www.sciencedirect.com/science/article/pii/S1001605809600433.
[14] C.M. Rhie, W.L. Chow, Numerical study of the turbulent flow past an airfoil with trailing edge separation, AIAA J. 21 (11) (1983) 1525–1532, http://dx.doi.org/10.2514/3.8284.
[15] S. Zhang, X. Zhao, General formulations for rhie-chow interpolation, 123, 2004, http://dx.doi.org/10.1115/HT-FED2004-56274.
[16] F.P. Karrholm, Rhie-chow interpolation in OpenFOAM, 2006, p. 7.
[17] D. Kim, H. Choi, A second-order time-accurate finite volume method for unsteady incompressible flow on hybrid unstructured grids, J. Comput. Phys. 162 (2) (2000) 411–428, http://dx.doi.org/10.1006/jcph.2000.6546, URL https://www.sciencedirect.com/science/article/pii/S002199910096546X.
[18] W. Yi, D. Corbett, X.-F. Yuan, An improved Rhie–Chow interpolation scheme for the smoothed-interface immersed boundary method, Internat. J. Numer. Methods Fluids 82 (11) (2016) 770–795.
[19] Y. Kawaguchi, W.-Q. Tao, H. Ozoe, Checkerboard pressure predictions due to the underrelaxation factor and time step size for a nonstaggered grid with momentum interpolation method, Numer. Heat Transf. B: Fundam. 41 (1) (2002) 85–94.
[20] J. Kim, I.-K. Park, H.K. Cho, Y. Yoon, J.J. Jeong, Collocated scheme on an unstructured mesh for two-phase flow analyses, in: Proceeding of Korean National Society Spring Meeting, Vol. 40, 2009, pp. 659–650.
[21] F. Denner, B. Wachem, A unified algorithm for interfacial flows with incompressible and compressible fluids, 2022.
[22] W.Z. Shen, J.A. Michelsen, J.N. Sørensen, Improved rhie-chow interpolation for unsteady flow computations, AIAA J. 39 (12) (2001) 2406–2409, arXiv:https://doi.org/10.2514/2.1252, URL https://doi.org/10.2514/2.1252.
[23] L. Hanimann, L. Mangani, M. Darwish, E. Casartelli, D.M. Vogt, A consistent and implicit rhie–chow interpolation for drag forces in coupled multiphase solvers, Int. J. Turbomach., Propuls. Power 6 (2) (2021) http://dx.doi.org/10.3390/ijtpp6020007, URL https://www.mdpi.com/2504-186X/6/2/7.
[24] P. Bartholomew, F. Denner, M.H. Abdol-Azis, A. Marquis, B.G. van Wachem, Unified formulation of the momentum-weighted interpolation for collocated variable arrangements, J. Comput. Phys. 375 (2018) 177–208, http://dx.doi.org/10.1016/j.jcp.2018.08.030, URL https://linkinghub.elsevier.com/retrieve/pii/S0021999118305539.
[25] R. Abgrall, How to prevent pressure oscillations in multicomponent flow calculations: A quasi conservative approach, J. Comput. Phys. 125 (1) (1996) 150–160, http://dx.doi.org/10.1006/jcph.1996.0085.
[26] I. Wenneker, A. Segal, P. Wesseling, A Mach-uniform unstructured staggered grid method, Internat. J. Numer. Methods Fluids 40 (9) (2002) 1209–1235, http://dx.doi.org/10.1002/fld.417, URL https://onlinelibrary.wiley.com/doi/10.1002/fld.417.
[27] F.H. Harlow, A.A. Amsden, A numerical fluid dynamics calculation method for all flow speeds, J. Comput. Phys. 8 (2) (1971) 197–213, http://dx.doi.org/10.1016/0021-9991(71)90002-7, URL https://www.sciencedirect.com/science/article/pii/0021999171900027.
[28] R. Saurel, F. Petitpas, R. Abgrall, Modelling phase transition in metastable liquids: application to cavitating and flashing flows, J. Fluid Mech. 607 (2008) 313–350, http://dx.doi.org/10.1017/S0022112008002061.
[29] V. Rusanov, The calculation of the interaction of non-stationary shock waves and obstacles, USSR Comput. Math. Math. Phys. 1 (2) (1962) 304–320, http://dx.doi.org/10.1016/0041-5553(62)90062-9, URL https://www.sciencedirect.com/science/article/pii/0041555362900629.
[30] S. Karni, Hybrid multifluid algorithms, SIAM J. Sci. Comput. 17 (1996) 1019–1039, http://dx.doi.org/10.1137/S106482759528003X.
[31] R. Saurel, R. Abgrall, A multiphase godunov method for compressible multifluid and multiphase flows, J. Comput. Phys. 150 (1999) 425–467, http://dx.doi.org/10.1006/JCPH.1999.6187.
[32] L. Zhang, A. Kumbaro, J.-M. Ghidaglia, A conservative pressure based solver with collocated variables on unstructured grids for two-fluid flows with phase change, J. Comput. Phys. 390 (2019) 265–289, http://dx.doi.org/10.1016/j.jcp.2019.04.007.
[33] R. Saurel, R. Abgrall, A multiphase godunov method for compressible multifluid and multiphase flows, J. Comput. Phys. 150 (2) (1999) 425–467, http://dx.doi.org/10.1006/jcph.1999.6187.
[34] R. Abgrall, R. Saurel, Discrete equations for physical and numerical compressible multiphase mixtures, J. Comput. Phys. 186 (2) (2003) 361–396, http://dx.doi.org/10.1016/s0021-9991(03)00011-1.
[35] J.-F. Haas, B. Sturtevant, Interaction of weak shock waves with cylindrical and spherical gas inhomogeneities, J. Fluid Mech. 181 (-1) (1987) 41, http://dx.doi.org/10.1017/S0022112087002003.
[36] F. Daude, P. Galon, On the computation of the Baer–Nunziato model using ALE formulation with HLL- and HLLC-type solvers towards fluid–structure interactions, J. Comput. Phys. 304 (2016) 189–230, http://dx.doi.org/10.1016/j.jcp.2015.09.056.